Published online 1 June 2016

Nucleic Acids Research, 2016, Vol. 44, No. 16 ***7673–7690***
doi: 10.1093/nar/gkw487

Chromosome thripsis by DNA double strand break clusters causes enhanced cell lethality, chromosomal translocations and 53BP1-recruitment

Agnes Schipler, Veronika Mladenova†, Aashish Soni†, Vladimir Nikolov, Janapriya Saha, Emil Mladenov and George Iliakis*

Institute of Medical Radiation Biology, University of Duisburg-Essen Medical School, 45122 Essen, Germany

Received April 17, 2015; Revised May 14, 2016; Accepted May 19, 2016

ABSTRACT

Chromosome translocations are hallmark of cancer and of radiation-induced cell killing, reflecting joining of incongruent DNA-ends that alter the genome. Translocation-formation requires DNA end-joining mechanisms and incompletely characterized, permissive chromatin conditions. We show that chromatin destabilization by clusters of DNA double-strand-breaks (DSBs) generated by the I-*Sce*I meganuclease at multiple, appropriately engineered genomic sites, compromises c-NHEJ and markedly increases cell killing and translocation-formation compared to single-DSBs. Translocation-formation from DSB-clusters utilizes Parp1 activity, implicating alt-EJ in their formation. Immunofluorescence experiments show that single-DSBs and DSB-clusters uniformly provoke the formation of single γ-H2AX foci, suggesting similar activation of early DNA damage response (DDR). Live-cell imaging also shows similar single-focus recruitment of the early-response protein MDC1, to single-DSBs and DSB-clusters. Notably, the late DDR protein, 53BP1 shows in live-cell imaging strikingly stronger recruitment to DSB-clusters as compared to single-DSBs. This is the first report that chromatin thripsis, in the form of engineered DSB-clusters, compromises first-line DSB-repair pathways, allowing alt-EJ to function as rescuing-backup. DSB-cluster-formation is indirectly linked to the increased biological effectiveness of high ionization-density radiations, such as the alpha-particles emitted by radon gas or the heavy-ions utilized in cancer therapy. Our observations provide the first direct mechanistic explanation for this long-known effect.

INTRODUCTION

The severity of double strand breaks (DSBs) as DNA lesions is evolutionarily ingrained in the wide spectrum of cellular responses elicited to this rather special form of DNA damage. When detecting DSBs, cells mount a network of responses collectively termed the 'DNA damage response (DDR)' (1) that modify nearly every metabolic activity of the cell. Not surprisingly, therefore, defects in DDR are associated with developmental, immunological and neurological disorders, and are a major driver of cancer (2). DDR is triggered by accidental DSBs generated by oxidative stress, DNA replication-errors (3–5), or ionizing radiation (IR), but also by programmed DSBs arising at specific locations in the genome during meiosis, as well as during V(D)J and immunoglobulin heavy chain class switch recombination (CSR) (6).

Despite the severity of DSBs as DNA lesions, higher eukaryotes have developed impressively efficient mechanisms for their removal from the genome (7,8). And yet, among DNA lesions, DSBs retain the highest probability for adverse biological effects including cell death, mutation, as well as transformation to a carcinogenic state. Notably, many of these adverse effects are caused by errors in processing that frequently manifest as chromosome translocations, i.e. by the joining of unrelated, incongruent DNA ends (6,9,10). In contrast to errors generated by DNA damage tolerance mechanisms, which have defined enzymatic underpinnings and mostly cause single base substitutions, translocations may be thought as rescue attempts following accidents in DSB processing. This view of events provokes inquiries in the sources of accidents and the identity of rescue-mechanisms recruited (6–11).

Pathways processing DSBs are broadly classified as homology-dependent and homology-independent (8,11–13). Homology-independent pathways function throughout the cell cycle and include the DNA-PK-dependent non-homologous end-joining (D-NHEJ; the term classical or canonical, c-NHEJ, is also frequently used and is adopted

*To whom correspondence should be addressed. Tel: +49 201 723 4152; Fax: +49 201 723 5966; Email: georg.iliakis@uk-essen.de
† Equal contribution

here), as well as an alternative end-joining pathway that under certain circumstances operates as backup to c-NHEJ and HRR, and is therefore termed alt-EJ, or B-NHEJ (8,14).

The most salient limitation of end-joining pathways is the absence of built-in mechanisms to reliably restore DNA sequence at the DSB and to ensure that only the original ends are rejoined. As a result, sequence alterations at the junction are frequent and translocation-formation possible (15). Although c-NHEJ and alt-EJ function on similar principles, alt-EJ is slower and less efficient and as a result more error-prone in the sense that it generates larger deletions and other sequence modifications at the junction, and has higher propensity to form translocations (6–11,16). Homology-dependent pathways, on the other hand, show strong cell cycle dependence and operate only when a sister chromatid becomes available after semi-conservative DNA replication. These pathways can faithfully restore DNA sequence at the DSB junction and are unlikely to cause translocations. As a result, end joining pathways are likely candidates for the processing of DSBs involved in accidents, with alt-EJ showing greater flexibility for this function than c-NHEJ (8,14).

A parameter frequently implicated as a source of processing accidents is the nature of the DSB. The definition of this parameter is necessitated by the fact that DSBs generated by physical or chemical agents can contain at the DNA-rupture site damaged sugar entities with lost or altered bases, as well as a spectrum of chemical alterations (DNA lesions) in the neighboring bases. The term DSB complexity is frequently used to specifically describe some of these characteristics (17).

While complexity is typically defined by the presence of additional lesions in the immediate vicinity of the DSB, DSB-clusters represent a further level of overall damage complexity that likely adds substantial excess-accident-risk to any processing attempt (8). Clusters of DSBs within a few hundred to several hundred-thousand base pairs will, depending on overall organization, destabilize chromatin and jeopardize its potential to orchestrate efficient processing of the constituent DSBs by all repair pathways (8). On the basis of their molecular constitution, DSB-clusters can be considered as a form of highly local chromothripsis—a phenomenon whereby as of yet undefined processes cause extensive localized genomic fragmentation (thripsis), which provokes inaccurate rejoining that feeds carcinogenesis (18–21).

There is experimental evidence for the induction of DSB-clusters under different experimental settings and conditions, most prominently though after exposure of cells to ionizing radiation (IR). Thus, DSB-clustering is considered the source of small DNA fragments visible by atomic force microscopy in irradiated cells (22) and is implicated in several adverse cellular radiation effects (23), including the direct suppression of c-NHEJ (24) (reviewed in (25)). Induction of DSB-clusters is more likely in cells exposed to radiation modalities of increasing ionization density (quantitatively described by the parameter: linear energy transfer, LET) (26–28), as in alpha-particles emitted from radon gas, or in heavy ions abundant in deep space and used in advanced treatment-centers of human cancer (29,30).

DSB-clusters and their contribution to the adverse effects of IR have been the subject of extensive mathematical modeling (25,31–33), under the hypothesis that such fragments will be lost from their chromatin context with probability that increases with decreasing fragment length (25,33–35), and will thus initiate many of the underlying detrimental radiation effects. Hence, analysis of effects elicited by DSB-clusters is important not only for our understanding of key aspects of the DNA damage response, but also in human health and space travel.

Notably, two processes essential for the maturation of the immune system are mediated by the programmed and highly regulated induction of a cluster of two DSBs, and in both processes the intervening DNA segment is lost (6,36), namely V(D)J recombination and CSR (37). Importantly, both processes pose oncogenic risks (38–41), which is compounded by the ability of antigen-receptor-locus regulatory-elements to activate expression of translocated oncogenes.

Despite the frequent hypothetical implication of DSB clustering in several adverse biological effects, direct analysis in defined model systems of the effects of DSB-clusters on DDR, genome stability and cell survival is lacking. Here, we address this void by testing the effects of especially designed, multiply genomically-integrated constructs modeling defined combinations of DSB-clusters. We present evidence for a hitherto undocumented potential of DSB-clusters, as compared to single-DSBs, to kill cells, cause chromosomal translocations and induce sustained DNA damage-signaling.

MATERIALS AND METHODS

Cell culture

Chinese hamster ovary (CHO) cell clones and DNA-PKcs deficient, XRC1-3, CHO clones with I-*Sce*I-transposon integrations as described below were grown in 100 mm culture dishes with 15 ml McCoy's 5A growth medium (Sigma-Aldrich), supplemented with 10% fetal-bovine serum (FBS), at 37°C in an atmosphere of 5% CO_2 in air. Exponentially growing cells were passaged every 2 days while maintaining a maximum confluence of about 75%. Cells with integrated I-*Sce*I transposon constructs were grown under selective pressure of 500 μg/ml G418.

Transfection by electroporation

To generate DSBs in cells with integrated I-*Sce*I sites, cells were transiently transfected with I-*Sce*I expressing plasmid pCMV3xnls-I*Sce*I, and were analyzed at the indicated times. Western blotting revealed that I-*Sce*I expression persists practically unchanged for at least 72 h post-transfection (Supplementary Figure S1A). There are no domains present on the I-*Sce*I protein used here that regulate localization or stability. The Amaxa Nucleofector® device (Lonza) was used for all transfection procedures according to the manufacturer's protocol by using program U-23. Briefly, 1×10^6–5×10^6 exponentially growing cells were transfected with pCMV3xnlsI-*Sce*I expression plasmid using 1 μg plasmid DNA per 10^6 cells. After transfection, cells were transferred to culture medium, pre-equilibrated and

pre-warmed in a CO_2 incubator for at least 30 min. Transfection efficiency was monitored by FACS, using a GFP-53BP1 expression plasmid.

Inhibitor treatments

Inhibitors were dissolved in dimethyl sulfoxide (DMSO) and were added to the culture medium immediately after transfection. The rather specific DNA-PKcs inhibitor NU7441 (IC_{50}-DNA-PKcs = 14 nM, IC_{50}-ATM > 100 μM, IC_{50}-ATR > 100 μM, IC_{50}-mTOR = 1.7 μM, IC_{50}-PI3K = 5.0 μM) was applied at a concentration of 5 μM. We addressed the question of cross reactivity of NU7441 for the special case of mTOR that has the lowest IC_{50}. Supplementary Figure S1B shows that treatment of two CHO clones (see below for more information) with 2.5 or 5 μM NU7441 fails to detectably affect phosphorylation of Akt at Serine-473, which is mTor dependent and therefore sensitive to 200 nM Torin1, a specific mTOR inhibitor. We conclude therefore that the effects of NU7441 treatment measured here, reflect practically exclusively the inhibition of DNA-PKcs. PJ34 inhibits mainly Parp1 and Parp2 members of the PARP-family, and was used at a concentration of 10 μM.

Ligation mediated PCR (LM-PCR)

For LM-PCR, genomic DNA was extracted 8 h after transfection of CHO-4xS.R11.C3 cells with pCMV3xnlsI-*Sce*I expression vector. Genomic DNA from non-transfected cells served as control. LM-PCR was carried out as described (42). Briefly, in the first step a double stranded linker was constructed and ligated to genomic DNA. The linker was generated by hybridizing the 25 bp (GCGGTGACCCGGGGAGATCTGAATTC) and 11 bp (GAATTCAGATC) oligonucleotides under gradually decreasing temperature. In the second step, a PCR was performed using a forward-primer complementary to the 25 bp linker sequence and the reverse-primer CACACCCTAACTGACACACATTC, which annealed, 110 bp downstream of the first I-*Sce*I recognition site. To increase the sensitivity of the LM-PCR assay, a second round a semi-nested PCR was performed with the reverse primer ACTTTCCACACCCTAACT (Figure 1E).

Vector construction and cloning

To generate transposon vectors harboring I-*SceI* integrations, a direct and reverse 200 bp 2xI-*Sce*I site sequences (2xS.Ds, 2xS.D, 2xS.R) were commercially procured from Sloning Biotechnology GmbH and delivered in the pPCRScript plasmids. The 4xS.R sequences were cloned using the 2xS sequence as a template. Four different primers were designed flanking the 2xS construct with additional restriction endonuclease sites for further cloning. In a first PCR, the 2xS sequence was amplified with primers containing an EcoRI site at the 5`end and SacII and SacI sites at the 3′ end. The amplicon was digested with EcoRI and SacI before ligation into the pPCRScript vector. In a second PCR, the two-site construct was amplified again to generate sequences with a different combination of restriction sites for further cloning (SacI at the 5`end and EcoRI and SacI at the 3`end). The PCR product was digested with SacI and subsequently cloned into the vector generated in the second step, already containing the PCR product of the first step. The SacII RE site in the final vector (pPCR-4xS) can be used for further cloning to increase the distance between the second and third I-*Sce*I site, for other types of insertions, or for additional construction strategies.

The vector containing a single I-*Sce*I site (1xS) was generated from the 2xS.D vector with I-*Sce*I sites in a direct orientation, after digestion with I-*Sce*I endonuclease and re-ligation of the restriction products.

Subsequent cloning of the 1xS, 2xS.D, 2xS.R and 4xS I-*Sce*I containing DNA fragments was performed in pT2/SVNeo transposon vector, by using the EcoRI sites. Supercoiled pT2/SVNeo plasmids with different I-*Sce*I integrations were prepared using CsCl/EtBr gradients. In the final step the plasmid–DNA pellet was dissolved in TE and dialyzed against TE buffer.

Colony forming assay

To assess the colony forming ability of CHO-clones after expression of I-*Sce*I, 200–1000 cells were plated in triplicates after transfection with pCMV3xnlsI-*Sce*I plasmid. Cells were grown for 9 days and stained with 1% crystal violet dissolved in 70% ethanol. Colonies were counted using a low magnification binocular microscope. Transfection with the GFP expressing plasmid GFP-53BP1 served as a control to estimate transfection efficiency. The transfection efficiency, was estimated by flow cytometry measurement of the GFP fluorescence signal, 24 h after transfection.

Classical cytogenetic analysis

To analyze formation of chromosomal aberrations, classical cytogenetic methods were employed. For metaphase analysis, 2.5×10^6 cells transfected with pCMV3xnls-I*Sce*I plasmid and 2.5×10^6 mock transfected cells were plated for 12 and 24 h, respectively. To accumulate cells at metaphase, colcemid (Biochrom AG) was added for 2 h at a concentration of 0.1 μg/ml. Cells were collected by trypsinization and were exposed for 5 min in 10 ml of hypotonic solution (75 mM, KCl). Subsequently cells were fixed in 10 ml, 3:1 methanol (Sigma Aldrich)/acetic acid (Carl Roth GmbH & Co.) and kept at 4°C overnight. After washing twice with fixative, metaphase spreads were prepared and stained with Giemsa staining solution (3% Giemsa, 1× Sörensen's buffer). In addition to manual scoring, an automated imaging system (MetaSystems) was used to obtain high quality images of metaphase chromosomes. For metaphase search the M-Search module of the Metafer software (MetaSystems, Altlussheim, Germany) using the 10× objective of a Zeiss microscope (AxioImager.Z2, Zeiss) was used. Metaphases were captured at a magnification of 63×, using the AutoCapt setting of the Metafer software. Images were analyzed using the Ikaros Software. Alternatively metaphases were also scored using a Leica bright field microscope equipped with a camera (Allied Vision Technology). For analysis, 100 metaphases were scored in each of three independent experiments. Results are shown as averages ± standard errors.

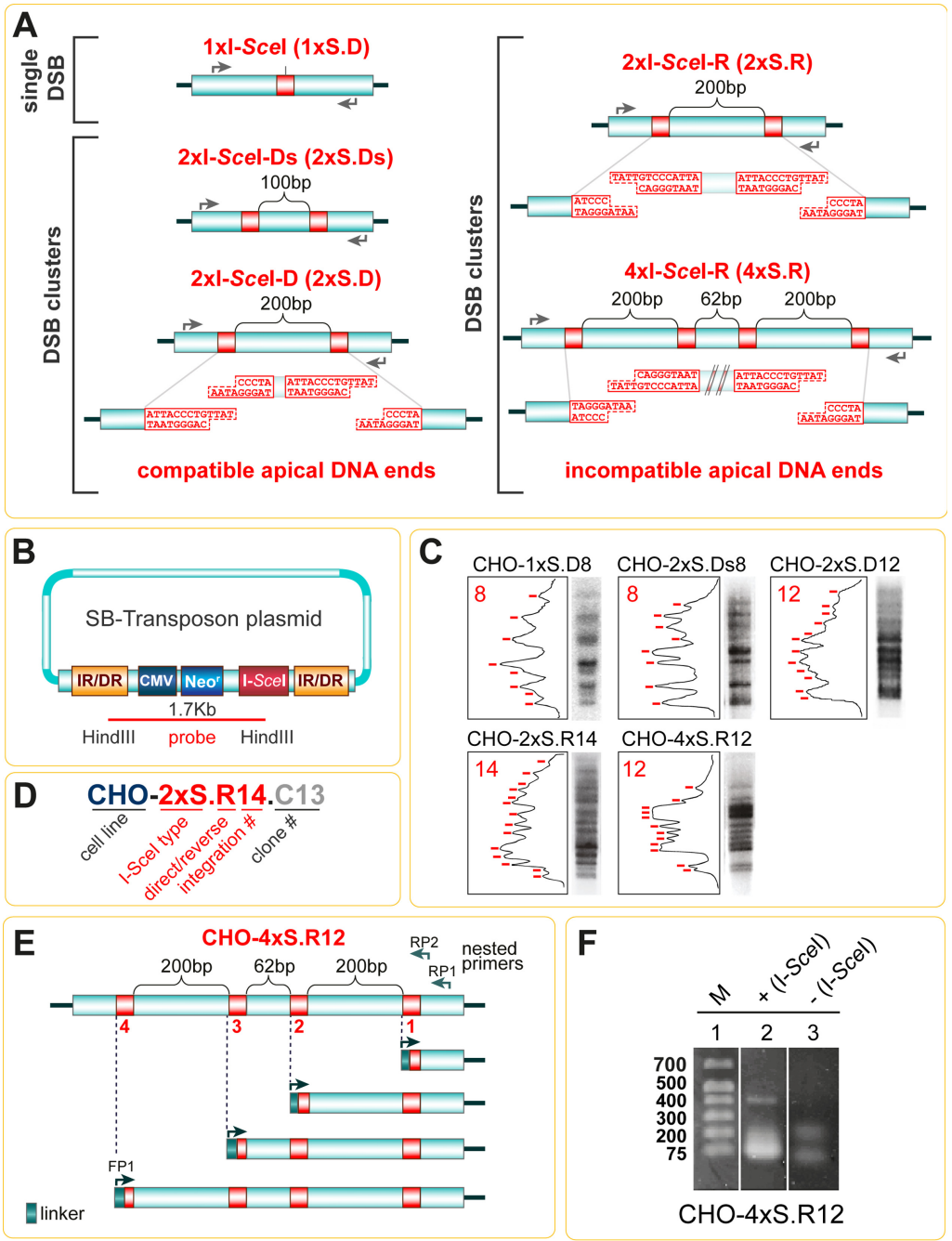

Figure 1. Approach to generate cell lines with multiple genomic integrations of I-*Sce*I constructs allowing induction of single-DSBs, or DSB-clusters. (**A**) Constructs carrying different combinations of I-*Sce*I sites engineered at specific distances and orientations. The schematics illustrate constructs allowing the generation of single-DSBs, of DSB-pairs at different distances (100 and 200 bp), as well as of DSB quadruplets. In constructs harboring two of more I-*Sce*I sites, the orientation between the sites (Direct: D or Reversed: R) is also indicated, as it results in the generation of compatible or incompatible apical DNA ends after loss of the intervening sequence. The grey arrows represent the locations of forward and reverse primers utilized to amplify the corresponding DNA segment for junction analysis by sequencing. (**B**) Map of the SB-transposon plasmid carrying the I-*Sce*I construct. The transposase binding sites comprising the IR/DR regions are shown. The region of the plasmid used as a probe in Southern blot analysis is indicated by the red line. CMV – cytomegalovirus promoter, Neo^r – neomycin resistance. (**C**) Southern blots analysis of CHO clones obtained after transfection with SB-transposon constructs harboring 1xS.D, 2xS.Ds, 2xS.D, 2xS.R and 4xS.R sites. The number of bands reflects the number of integrations. The densitometry plots on the left show the quantification basis regarding number of integrations in each clone. (**D**) Outline of the conventions used to name the clones employed in the present work. After the name of the parental cell line (CHO, or XRC1-3), the type of the integrated construct (1xS, 2xS and 4xS) is given, followed by information regarding the relative orientation of the apical I-*Sce*I sites (D-direct or R-reverse). The Ds abbreviation indicates the direct orientation of two I-*Sce*I sites separated by a shorter distance of 100 bp—instead of the typical distance of 200 bp used in other pairs. The number immediately after orientation represents the number of I-*Sce*I integrations detected in the clone (shown in C for CHO cells). The last component of the name refers to the specific clone (Cx) and is omitted for simplicity in the description of the results. (**E**) Outline of the ligation-mediated PCR (LM-PCR) using the 4xS.R construct in the CHO-4xS.R12 clone. Possible outcomes, as well as the forward and reverse primers used in the reaction are indicated. (**F**) Agarose gel electrophoresis showing LM-PCR products before and after I-*Sce*I cleavage. M, indicates DNA size markers.

Southern blotting

For Southern blotting, genomic DNA was isolated from CHO cells using DNAeasy Blood & Tissue Kit (Qiagen) according to the manufacturer's protocol. Restriction endonuclease digestion was accomplished with 20 μg genomic DNA and 6 μl Fast Digest XbaI restriction endonuclease (Thermo-Fisher). Digested genomic DNA was precipitated with three volumes of EtOH and run on 0.8% agarose gel prepared in TAE buffer. After resolving the DNA for 3–4 h at 0.2–0.3 V/cm, agarose gel was treated with depurination solution (0.2 M HCl) for 7 min, rinsed twice for 15 min in denaturation solution (1.5 M NaCl and 0.5 M NaOH) and neutralized with neutralization buffer (1 M Tris, pH 7.4 and 1.5 M NaCl). To transfer the DNA from the agarose-gel to the positively charged nylon membrane a standard capillary transfer devise was built. After 24 h of transfer, the nylon membrane was rinsed in ultrapure water and equilibrated in 6× SSPE for 10 min. To crosslink the DNA, the membrane was heated for 50 min at 110°C.

A 1.72 kb fragment of the integrated transposon construct served as probe (Figure 1B). To radioactively label the hybridization probe, the Prime-It II Random Prime Labeling Kit (Agilent Technologies) was used and radioactive nucleotides ([α-^{32}P]-dCTP at 3000 Ci/mmol) were incorporated into the newly synthesized strand according to the manufacturer's instructions. The activity of the probe was determined by liquid scintillation counting. For hybridization, the QuikHyb Hybridization Solution (Agilent Technologies) was used according to the manufacturer's protocol. Hybridization was carried out at 58°C, overnight. After low- and high-stringency washes, membrane was briefly rinsed in 0.1x SSPE at RT, wrapped in saran wrap and exposed for 48 h to a storage phosphoimaging screen (GE-Healthcare). The phosphoimaging screen was scanned in a Typhoon^{TM} Variable Mode Imager (GE-Healthcare).

SDS-PAGE and western blot analysis

Protein extracts for western blot experiments were prepared by using RIPA buffer (Thermo-Fisher), according to the manufacturer's instructions. SDS-PAGE was carried out in 10% polyacrylamide gels using standard protocols. For western blot analysis proteins were transferred onto nitrocellulose membranes using wet-transfer. Equal loading and transfer efficiency were monitored by immunodetection of GAPDH. After transfer, the membranes were incubated in blocking buffer (5% non-fat dry milk in 0.1% Tween-20, 150 mM NaCl, 25 mM Tris–HCl, pH 7.6) for 1 h at room temperature or overnight at 4°C, followed by overnight incubation with primary antibody at 4°C. Membranes were washed three times for 10 min with TBS-T (0.1% Tween-20, 150 mM NaCl, 25 mM Tris–HCl, pH 7.6) and incubated for 1 h with secondary antibody.

The following primary antibodies were used: anti-Akt-pS473 (Santa Cruz) (Ab1), anti-Akt-pS473 (Thermo-Fisher) (Ab2) and anti-GAPDH mouse monoclonal antibody (Merck Millipore). The secondary antibodies were: anti-mouse IgG conjugated with IRDye680 (Li-COR) and anti-rabbit IgG conjugated with IRDye800 (Li-COR). The proteins on the membranes were visualized by scanning using Odyssey infrared imaging scanner (Li-COR).

Immunofluorescence staining

For indirect immunofluorescence staining analysis, 0.3 × 10^6 transfected cells were plated in 35 mm dishes. Twelve hours after transfection cells were washed with PBS and fixed in 2% paraformaldehyde (PFA) for 15 min. Cells were washed and permeabilized in P-solution (100 mM Tris, pH 7.4, 50 mM EDTA, 0.5% Triton X-100) for 5 min and subsequently incubated in PBG blocking buffer (0.2% gelatin, 0.5% BSA in PBS) at 4°C overnight. The primary antibody was diluted 1:400 in PBG buffer and the cover slips were incubated for 2 h at RT. After washing 3 × 10 min with PBS, cells were incubated for 1.5 h with the secondary antibody diluted 1:400. After DNA counterstaining with 0.025 μg/ml DAPI solution, cells were mounted in 10 μl Promofluor antifade mounting media (PromoKine) and processed for scanning on a Confocal Laser Scanning Microscope (TCS SP5, Leica Microsystems). The following antibodies were used: anti-γ-H2AX [3F2] mouse monoclonal antibody (Abcam PLC), anti-53BP1 rabbit polyclonal antibody (Santa Cruz), anti-mouse IgG antibody conjugated with AlexaFluor 488 and anti-rabbit IgG antibody, conjugated with AlexaFluor568 (Life Technologies).

Live cell imaging

Live cell imaging was used to monitor dynamic nuclear events over a time period of 20 h. Parallel to laser scanning microscopy, differential interference contrast (DIC) was applied to observe cell viability and morphology together with foci kinetics. During live cell imaging, cells were cultured in L-15 Leibovitz`s Media and were maintained in a temperature-controlled chamber at 37°C. Experiments were carried out with transiently transfected cells that express GFP-tagged repair proteins (53BP1 or MDC1). 0.3 × 10^6 transfected cells were plated in each well of an eight-well plate (PAA). Four hours after plating, cells were washed twice with pre-warmed PBS and transferred to pre-warmed L-15 Leibovitz media. A 63× water-immersion objective connected to a Water Immersion Micro Dispenser (Leica) was used. The controlled MP6-pump (Bartels Mikrotechnik) was set at a pump-amplitude of 75 V, pumping 279 μl water every 25 min for 10 s. GFP was measured by excitation with 488 nm argon laser with a laser power set to 30% to reduce photobleaching. In total 16 fields were tracked at time intervals of 1 h for 20 h

Quantitative analysis of DSB repair foci

The analysis of the generated images was performed using the Imaris® software (Imaris 7.0; Bitplane). Movies were generated with the 'Easy-3D' tool allowing analysis of foci kinetics in a spatio-temporal resolution. For foci scoring, images of 1 h time frames, from 4 to 20 h after transfection, were loaded and foci of 100 cells were counted for each time point. Foci were defined as spots of intensity higher than the defined threshold, with a minimum size of 0.5 μm. The same routine was applied to evaluate the number of repair foci in indirect immunofluorescence experiments.

Alternatively, the number of γ-H2AX and 53BP1 foci were assessed by an automated image analysis at MetaSys-

tems imaging system using MetaCyte mode of the Metafer 4 software.

Junction sequencing and analysis of sequencing data

To sequence the junctions generated after processing of DSBs induced by I-*Sce*I, a genomic DNA from each transfected CHO clone was isolated by using a genomic DNA tissue kit (Macherey-Nagel). PCR reaction with primers flanking the I-*Sce*I sites as shown in Figure 1A was used to amplify the corresponding DNA segments for sequencing. PCR products were cloned into pGEM T-Easy vector (Promega) to generate a single copy of the PCR fragment. pGEM T-Easy vectors were transfected into DH5α competent bacterial and transformed clones generated on ampicillin agar plates. Several bacterial clones generated for each cell clone were collected and sent for Sanger-sequencing using the forward primer from the PCR reaction. Sequencing data were aligned with the MUSCLE multiple alignment algorithm integrated in the U-gene free software package for computational DNA analysis.

RESULTS

Design of I-SceI constructs for the controlled induction of DSB-clusters in the mammalian genome

To study the biological consequences of DSB-clustering, we generated rodent cell lines harboring in their genomes multiple copies of different-size-clusters of I-*Sce*I recognition sites (43), engineered at orientations leading to the formation of compatible or incompatible apical ends upon digestion. A single I-*Sce*I site (1xI-*Sce*I-D) represents the simplest directly ligatable form ('D') and serves as control 'single-DSB' in this model system (8) (Figure 1A).

The next construct comprises a pair of I-*Sce*I recognition sequences, engineered 200 bp apart, which are either directly oriented to generate ligatable apical ends (2xI-*Sce*I-D, Figure 1A, left panel), or placed in reverse orientation to generate incompatible apical ends (2xI-*Sce*I-R, Figure 1A, right panel). The highest level of clustering investigated comprises quadruplets of I-*Sce*I-sites engineered at an overall distance of 462 bp, either in direct orientation (4xI-*Sce*I-D, not included), or in reverse orientation at the apical ends (4xI-*Sce*I-R, Figure 1A, right panel).

During the generation of cell clones with the above constellations of I-*Sce*I clusters, a fortuitous genetic rearrangement during plasmid propagation produced a construct with a pair of I-*Sce*I sites spaced 100 bp apart, instead of the aimed 200 bp, in direct orientation (2xI-*Sce*I-Ds, where '*s*' denotes the shorter intervening sequence) (2xI-*Sce*I-Ds, Figure 1A, left panel). A cell clone with this form of integrated construct is included in the present analysis.

Transient expression of I-*Sce*I, in cells with genomically integrated constructs of the types shown in Figure 1A, will rupture chromatin by generating either single-DSBs, or DSB-clusters, which will cause increasing levels of local chromatin 'thripsis'. At each individual I-*Sce*I site, restriction by I-*Sce*I may be followed by multiple cycles of ligation and re-cutting (44), which for DSB-clusters may be compounded by occasional intervening-fragment-loss, although the model system is not specifically selecting for such events. Distances between adjacent I-*Sce*I sites were chosen approximately equal to the average nucleosomal DNA length in chromatin (200 bp) reasoning that this may increase the probability of fragment loss in the DSB-cluster. The clone with the I-*Sce*I pairs located only 100 bp apart allows a first direct test of this rationale.

Each thripsis-event is considered here as a *single* chromatin-rupture event of 'complexity' proportional to the number of DSBs involved. Chromatin restitution may occur by ligation of directly proximal, as well as of the more stable (in the chromatin context) apical DNA ends, but also by a number of other non-canonical processes that are described below and underpin the negative biological consequences studied.

Clonal cell lines with multiple genomic integrations of constructs with I-SceI-site-clusters

CHO10B4 cells were selected for genomic integration of the constructs shown in Figure 1A owing to their excellent growth characteristics and the availability of DNA repair mutants that allow genetic analysis of the elicited responses. Here, in addition to wt CHO cells, clones with stably integrated I-*Sce*I constructs were generated in the XRC1-3 mutant, lacking DNA-PKcs activity.

A key step in the development of the present model system is the generation and characterization of clonal cell lines with multiple integrations of each construct to allow, similar to IR-exposure, the induction in each cell of multiple DSBs or DSB-clusters, and the analysis of their consequences on cell survival, genome stability and DDR.

To achieve multiple I-*Sce*I-construct integrations in the genome of the selected cell lines, we utilized the Sleeping-Beauty (SB) transposon system (45,46). The SB transposon has been genetically reconstructed from teleost fish and mediates efficient chromosomal integration of DNA sequences by a cut-and-paste mechanism (45,46). Specifically, SB-transposition is based on two non-autonomous transposon elements: the transposon-donor plasmid, pT2/SVNeo (Supplementary Figure S2A), and the hyperactive SB-transposase-expressing, helper-plasmid pCMV(CAT)SB100x, which catalyzes the transposition event (Supplementary Figure S2B). For efficient genomic integration at multiple copies by transposition, I-*Sce*I constructs (Figure 1A) are cloned into pT2/SVNeo plasmid between the inverted/direct-repeats (IR/DRs) at the EcoRI restriction site (Figure 1B) and co-transfected with pCMV(CAT)SB100x.

Expanded, *neo*-resistant clones are analyzed by Southern blotting to determine the number of integrations (Figure 1C). As 'probe' serves a 1.72 kb segment encompassing 121 bp of the I-*Sce*I recognition sequence, as well as the neomycin resistance gene and the CMV promoter (red line in Figure 1B). The number of integrations detected visually, as well as by densitometry (Figure 1C), denotes the number of single-DSBs or DSB-clusters that may be generated in each clone upon expression of I-*Sce*I via transfection of pCMV3xnls-I*Sce*I plasmid.

From a pool of integration-characterized clones we selected the following for the experiments described below (See Figure 1D for cell line nomenclature-conventions):

CHO-1xS.D8.C12 (CHO clone 12, with eight integrations of a single I-*Sce*I site), CHO-2xS.Ds8.C2 (CHO clone 2, with eight integrations of I-*Sce*I site duplets at the shorter distance of 100 bp in direct orientation generating compatible apical ends), CHO-2xS.D12.C8 (CHO clone 8, with twelve integrations of I-*Sce*I site duplets separated by 200 bp in direct orientation generating compatible apical ends), CHO-2xS.R14.C13 (CHO clone 13, with fourteen integrations of I-*Sce*I site duplets separated by 200 bp in reverse orientation generating incompatible apical ends), CHO-4xS.R12.C3 (CHO clone 3, with 12 integrations of I-*Sce*I site quadruplets comprising two pairs separated by 62 bp in an orientation generating incompatible apical ends), XRC1-3-2xS.D10.C7 (XRC13 clone 7, a DNA-PKcs mutant, with 10 integrations of I-*Sce*I site duplets separated by 200 bp in direct orientation generating compatible apical ends) and XRC1-3-2xS.R10.C1 (XRC13 clone 1, with ten integrations of I-*Sce*I site duplets separated by 200 bp in reverse orientation generating incompatible apical ends). To simplify cell line designation in the remainder of the paper we will omit the designation of the clone—last position in Figure 1D.

Cleavage of individual I-*Sce*I sites in the integrated constructs can be assessed by ligation-mediated PCR (LM-PCR). This is shown in Figure 1E for CHO-4xS.R12-cells analyzed 8 h after I-*Sce*I-plasmid transfection. In the first step of LM-PCR, a double stranded linker DNA is ligated to I-*Sce*I-restricted, genomic DNA; in unrestricted DNA this ligation is not possible and thus signal cannot be generated in the following amplification step. In the second step, a PCR is performed using as forward primer 1 (FP1) an oligonucleotide complementary to a region of the ligated linker and as reverse primer 1 (RP1) an oligonucleotide complementary to the 110 bp region downstream of the outer I-*Sce*I segment (Figure 1E). To increase assay sensitivity, a second semi-nested PCR is performed using RP2 (Figure 1E).

In the absence of I-*Sce*I expression, two faint, background bands of ∼80 and 260 bp are detected. After I-*Sce*I expression, a strong band of about 80 bp appears, reflecting efficient restriction of the first site left to RP1. Beyond background bands, here also a band of ∼400 bp is detected, as well as a faint band of ∼500 bp. Generation of these larger-size bands requires restriction of I-*Sce*I sites 3 or 4 but intact (unrestricted) sites 1 and 2 (Figure 1E). The latter requirement is evidently infrequently fulfilled (i.e. sites 1 and 2 are frequently restricted) and as a result these bands are faint, while a 300 bp band from restriction of site 2 alone is completely absent. Collectively, the results demonstrate effective, simultaneous restriction of multiple I-*Sce*I sites in the integrated constructs and thus the generation of DSB-clusters in the cellular genome.

DSB-clusters are markedly more efficient than single-DSBs in killing cells

Our experimental model allows direct and specific comparison between the biological consequences of single-DSBs and DSB-clusters in the genome of mammalian cells. SSBs and base damages, which far outnumber DSBs in cells exposed to IR (8), and contribute to cell lethality and translocation-formation to degrees that cannot be quantitatively separated from those of DSBs, are not confounding factors since they are completely absent in our model system.

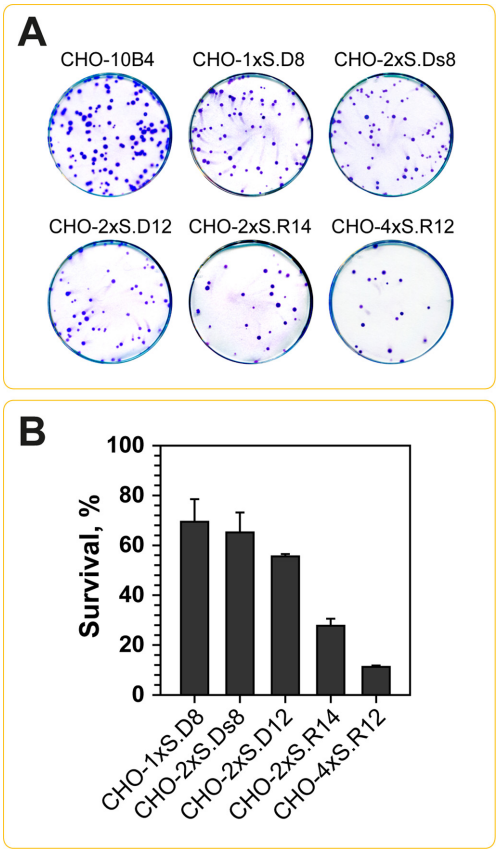

Figure 2. DSB-clusters kill cells more efficiently than single-DSBs. (**A**) Representative cell culture dishes showing colonies forming after transient expression of I-*Sce*I in different CHO clones as indicated, as well as in the parental CHO-10B4 cell line. For each dish, 150 cells were plated immediately after transfection and incubated for 7–8 days to allow colony formation. (**B**) Survival of transfected cells calculated using the plating efficiency measured in mock-transfected cells of the same clone. Results represent average ± standard error (SE) calculated from three independent experiments. Transfection efficiency was monitored by parallel transfection with pGFP-53BP1 plasmid and analysis by flow cytometry 24 h later. Only experiments with transfection efficiencies higher than 85% (which was typical) are included in the analysis.

Figure 2A shows typical colony formation for the parental CHO10B4 cells, as well as the clones CHO-1xS.D8, CHO-2xS.Ds8, CHO-2xS.D12, CHO-2xS.R14 and CHO-4xS.R12 when plated immediately after transfection for transient I-*Sce*I expression to generate the corresponding DSB-clusters. Figure 2B summarizes compiled cell survival results from three experiments. For each clone, mock-transfected cells were to determine plating efficiency, typically 80–85%, which is used to calculate the net effect of I-*Sce*I expression—shown as survival in the figure. Transfection efficiency is also determined in each experiment using the GFP-53BP1 plasmid and is typically 70–90%.

Single-DSBs and DSB-pairs separated by 100 bp cause relatively low cell killing (∼30%), suggesting limited efficacy in generating lethal events. DSB pairs with compatible apical ends separated by 200 bp cause slightly more

cell killing (~40%). This likely reflects the higher number of DSB-clusters induced in this clone (12 versus 8).

Notably, a significant increase in cell killing (to 70%) is observed with a comparable number of DSB-pairs in the clone where incompatible apical ends are generated (CHO-2xS.R14).

Strikingly, DSB quadruplets with incompatible ends kill over 90% of cells on average. This high degree of killing becomes even more impressive when one considers that transfection efficiency is less than 100% and that untransfected cells will not sustain DSBs and will therefore survive. Thus, the vast majority of cells harboring I-*Sce*I-quadruplets and sustaining therefore DSB clusters of this complexity after I-*Sce*I expression, likely succumb to this form of DNA damage.

Collectively, the above observations converge to the following conclusions: (i) DSB-clusters are more likely to confer lethality than single-DSBs; (ii) the risk of cell death increases with increasing number of DSBs per cluster; (iii) lethality is significantly higher when incompatible apical ends are generated in the cluster, as compared to compatible ends.

To elucidate the molecular underpinnings of this response we examined next DSB-processing within DSB-clusters by analyzing junction-formation, utilizing molecular biology and cytogenetic approaches.

Processing of DSB-clusters causes deletions at the junctions at frequencies increasing with increasing DSB-number per cluster

To evaluate processing fidelity of single-DSBs and DSB-clusters, we transfected I-*Sce*I in the above clones and collected cells 24 h later for junction analysis. To this end, we prepared genomic DNA from the transfected cell pool and amplified by PCR the segments encompassing the I-*Sce*I clusters using the primers indicated by the grey arrows in Figure 1A. Analysis of this segment specifically assesses events that restore the site and allows characterization of occasional sequence alterations. Unprocessed breaks and processing leading to the rejoining of unrelated ends preclude product formation in this form of PCR and remain therefore undetected.

PCR products are cloned into pGEM T-Easy vector and used to transform competent bacteria. Bacterial clones are expanded and cloned DNA segments sequenced to characterize possible alterations at the junction. The results obtained for the four CHO clones carrying different constellations of DSB-clusters are summarized in Figure 3. Shown are results obtained after sequencing of 12–25 junctions per clone.

With single-DSBs (Figure 3A) and DSB-pairs (Figure 3B and C) the majority of sequenced junctions shows restitution of the I-*Sce*I site. In the few cases where the junction is altered, deletion of the DNA segment between the I-*Sce*I sites is observed. This picture is completely changed when junctions from the clone harboring DSB-quadruplets are analyzed (Figure 3D). Here, the majority of analyzed junctions shows losses of DNA segments between I-*Sce*I sites and at times even of DNA segments extending beyond these boundaries.

Table 1. Fraction of undamaged metaphases in the different cell clones. The values are average ± SE from three independent experiments

Normal Metaphases at 24h		
	Average	**SE**
CHO-1xS.D8	65.3	7.2
CHO-2xS.Ds8	64.0	4.0
CHO-2xS.D12	55.5	7.5
CHO-2xS.R14	30.7	5.0
CHO-4xS.R12	32.7	4.2

The trends noted above are summarized in Figure 3E that shows the sum of all alterations detected at the junction and includes results of similar experiments carried out with the XRC1-3 clones. It is notable that nearly all junctions generated from DSB quadruplets are altered and that junctions generated at DSB pairs or DSB singlets show less alterations. Junction alterations are slightly more frequent in the DNA-PKcs deficient XRC1-3 cells.

We conclude that DSB-clusters are likely to loose during processing the DNA segments between I-*Sce*I sites and consider this trend an indication of their inherent instability. This form of instability increases markedly with increasing number of DSBs in the cluster. Base substitutions or single base losses, while detectable with all I-*Sce*I constellations tested, they remain infrequent in the sequencing results.

While indicative and with clear trends, the above results cannot directly explain cell survival outcomes because deletions and other junction-alteration-events, such as those described above, affect non-essential DNA sequences, loss or alteration of which are unlikely to cause lethality. Therefore we extended our experiments to include cytogenetic analysis of the cellular genomes.

DSB-clusters are markedly more efficient than single-DSBs in generating chromosome aberrations

Cell killing after IR correlates with the formation of chromosome aberrations (47). We investigated chromosome aberration formation at metaphase in the above clones, 12–24 h after I-*Sce*I expression. As a first step, metaphases from each clone were inspected and classified as aberrant or normal depending upon whether visible chromosomal aberrations were present or not. Table 1 summarizes the results obtained and shows that the percentage of normal metaphases drops from 65% in cells harboring single-DSBs to 32% in cells harboring DSB-quadruplets. Figure 4A shows representative metaphases from these clones and demonstrates the formation of chromatid breaks and chromatid/chromosome translocations at numbers and complexities that increase with increasing DSB-clustering.

For a quantitative analysis of chromosome damage, we scored separately two types of chromosomal abnormalities:

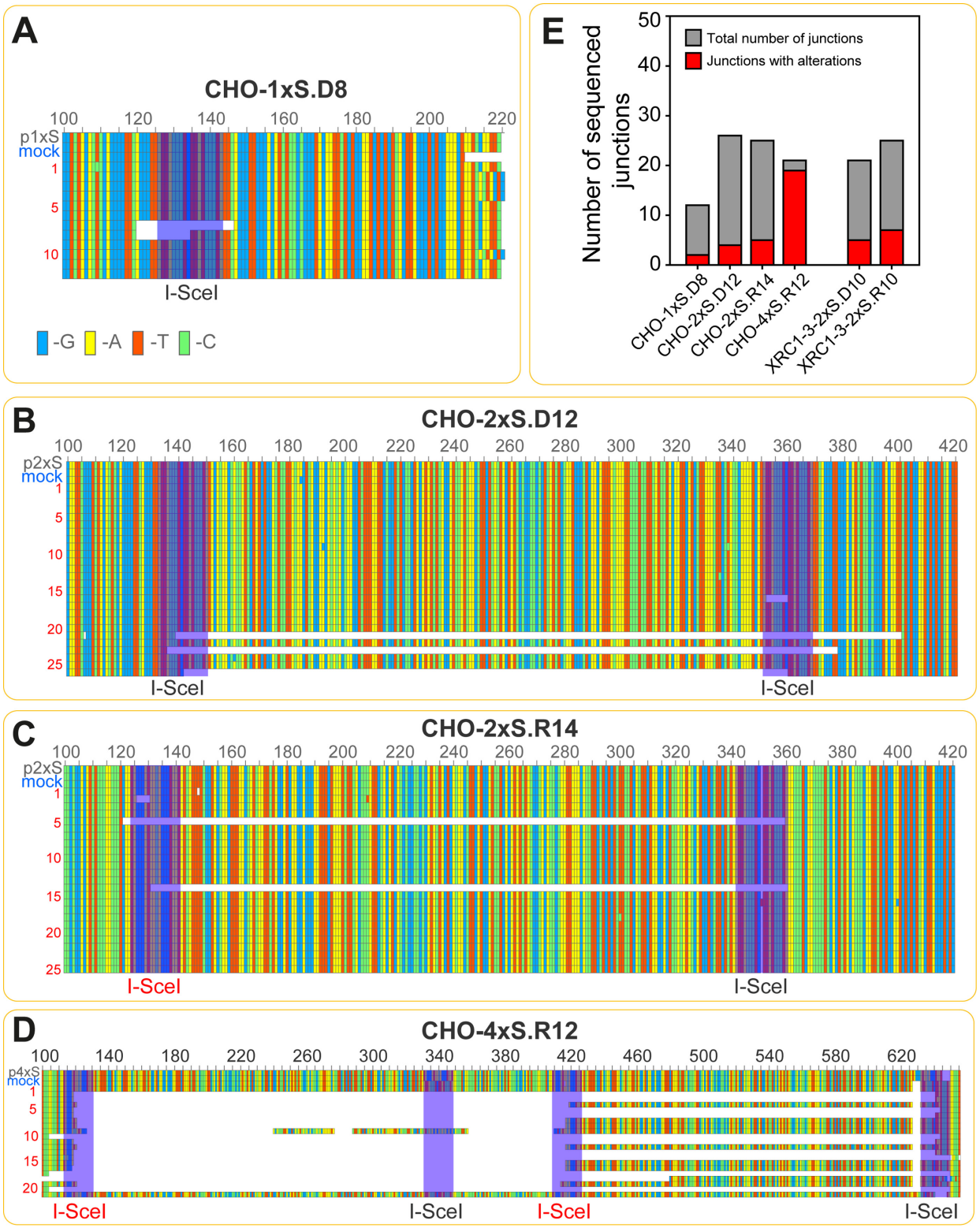

Figure 3. Junction analysis by sequencing in CHO cells harboring single I-*Sce*I sites and I-*Sce*I clusters. DNA segments defined by primers flanking the I-*Sce*I sites as shown in Figure 1A were amplified from genomic DNA isolated from the corresponding clones 24 h after transfection with the I-*Sce*I expression plasmid. PCR products were processed and analyzed as outlined under 'Materials and Methods'. 12–25 bacterial clones carrying individual PCR fragments were analyzed for each CHO clone. (**A**) Analysis of junctions generated in the CHO-1xS.D8 clone. Individual DNA bases are colored as follows: guanine (G)-blue, adenine (A)-yellow, thymidine (T)-red, cytidine (C)-green. The white gaps represent deleted DNA segments. As consensus DNA sequence, the I-*Sce*I construct shown in Figure 1A was utilized and is the top line in each map. (**B**), (**C**) and (**D**) As in panel A, for CHO-2xS.D12, CHO-2xS.R14 and CHO-4xS.R12, respectively. (**E**) Quantitative analysis of the results obtained in all clones analyzed. Shown is the total number of junctions sequenced for each clone together with the number of junctions showing sequence alterations.

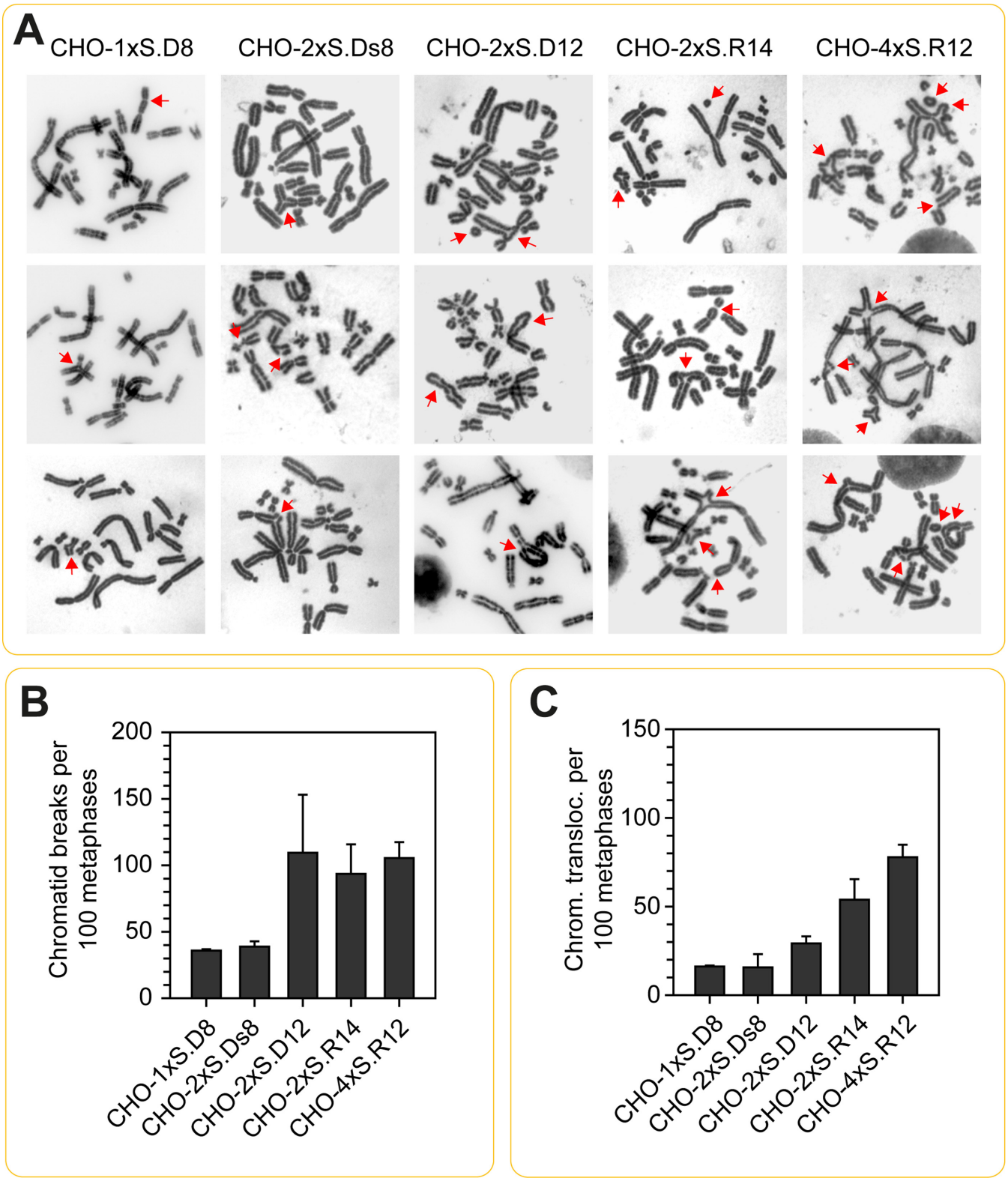

Figure 4. DSB-clusters generate more chromosomal aberrations than single-DSBs. (**A**) Images of selected metaphases of the indicated CHO clones captured 24 h after transfection with the I-*Sce*I expression plasmid. Red arrows point to chromosomal aberrations. (**B**) Quantitative analysis of chromatid break formation. Chromatid breaks scored in mock transfected cells have been subtracted (0–14 per 100 metaphases). Shown are results from three independent experiments as average ± SE. (**C**) Chromosomal translocations scored in the different clones as indicated. Results from three independent experiments are shown as average ± SE. Chromosomal translocations scored in mock-transfected cells have been subtracted (0–4 per 100 metaphases).

chromatid breaks reflecting mainly unprocessed DSBs, and chromosome/chromatid translocations reflecting processing in an error-prone manner.

Figure 4B shows modest incidence of chromatid breaks in CHO-1xS.D8 cells harboring single-DSBs and in CHO-2xS.Ds8 cells harboring DSB pairs separated by 100 bp. Notably, the incidence of chromatid breaks more than doubles in CHO-2xS.D12, CHO-2xS.R14 and CHO-4xS.R12 demonstrating that DSB-clustering with the selected separation geometry increases the probability of chromatin rupture. DSB pairs and quadruplets show similar chromatid rupture potential independently of apical end compatibility.

Collectively, these results suggest a weak correlation between cell killing and the induction of chromatid breaks in cells sustaining single-DSBs or DSB-clusters. We reasoned that this is because chromatid breaks may be rejoined at later times without affecting cell viability. Therefore, we hypothesized that the increased lethality noted in Figure 2A and B for certain constellations of DSB-clusters derives from detrimental gross genomic rearrangements such as those shown in the representative metaphases of Figure 4A. To test this hypothesis we scored chromosomal translocations under the same conditions and the results obtained are summarized in Figure 4C.

While low levels of chromosomal translocations are detected in the clones harboring 8 integrations of single I-*Sce*I sites or I-*Sce*I pairs separated by 100 bp, a statistically significant increase is noted in the clone harboring 12 I-*Sce*I pairs with compatible apical ends. Further increase is noted when 14 DSB pairs with incompatible ends are generated (CHO-2xS.R14 clone). Notably, the highest incidence of chromosome translocations is found in the CHO-4xS.R12 clone harboring 12 DSB-quadruplets. We conclude that DSB-clusters kill cells by destabilizing chromatin thus generating gross genomic rearrangements, frequently manifesting as chromosomal translocations.

DSB-clusters abrogate c-NHEJ function and are frequently processed by alt-EJ

The above results on cell lethality, junction restoration and chromosome aberration formation in cells sustaining single-DSBs and DSB-clusters, immediately raise questions regarding the repair pathways engaged and their involvement in the formation of lethal genomic rearrangements. To address this question we analyzed similar responses using small molecule inhibitors targeting components of selected end-joining repair pathways, and examined the effects of similar constellations of DSBs in the c-NHEJ mutant XRC1-3.

NU7441 is a specific inhibitor of DNA-PKcs, a key component of c-NHEJ. Treatment of CHO-1xS.D8 cells harboring single-DSBs with NU7441 causes an increase in translocation-formation by over a factor of two (Figure 5A and B). An increase in translocation-formation by over 50% is also observed with CHO-2xS.Ds8 harboring DSB pairs engineered 100 bp apart. Also treatment with NU7441 of CHO-2xS.D12 or CHO-2xS.R14 cells harboring 12 or 14 DSB-pairs located 200 bp apart in compatible or incompatible orientation, respectively, causes an over twofold increase in translocation-formation (Figure 5A and B). Collectively, these results suggest that cells process single-DSBs and DSB-pairs using c-NHEJ, and that pharmacological inhibition of c-NHEJ impairs normal processing and shunts these lesions to more error-prone pathways, such as alt-EJ, increasing thus the incidence of chromosomal translocations. Single DSBs and DSB pairs show here similar switching propensities from c-NHEJ to alt-EJ, as evidenced by the similar increase in translocation formation upon c-NHEJ inhibition.

Strikingly, treatment with NU7441 of cells harboring DSB-quadruplets generating incompatible apical ends, CHO-4xS.R12, has only a minor effect on translocation-formation suggesting that with increasing DSB-clustering the engagement of c-NHEJ is inherently compromised and lesions are shunted by default to error-prone repair pathways (alt-EJ) – thus blunting the effect of pharmacological c-NHEJ inhibition through NU7441.

The above conclusions are also supported by the results obtained by inserting in the DNA-PKcs mutant of CHO, XRC1-3, ten I-*Sce*I pairs in compatible or incompatible orientation, XRC1-3-2xS.D10 and XRC1-3-2xS.R10, respectively. The red bars in Figure 5A show that in these clones chromosomal translocations form, in the absence of any inhibitor, at levels very similar to those observed in their wild-type parental cell line after treatment with NU7441—particularly after considering the slightly lower numbers of DSB pairs this mutant harbors.

To further explore the reduced contribution of c-NHEJ and the presumed concomitant increase in the contribution of alt-EJ with increasing DSB clustering, we scored translocation-formation in the presence of a small molecule inhibitor (PJ34) of Parp1, a factor implicated in alt-EJ (16,44,48,49). PJ34 has no effect, or has only a small effect on translocations forming from single-DSBs and DSB-pairs located 100 bp apart. A stronger PJ34 effect is noted for DSB pairs located 200 bp apart either when they present in direct or in inverse orientation. Notably, PJ34 has a strong inhibitory effect on translocations forming in cells harboring DSB-quadruplets (Figure 5C).

We conclude that in the case of single-DSBs and DSB-pairs, c-NHEJ protects cells from chromosome translocation-formation and that inhibition of this repair pathway using NU7441 causes alt-EJ-mediated increase in translocation formation. In contrast, c-NHEJ is inherently compromised in the case of DSB-quadruples, which are constitutively processed by alt-EJ giving rise with high probability to chromosomal translocations. Thus, local chromothripsis compromises c-NHEJ giving alt-EJ opportunities for function.

Single-DSBs and DSB-clusters initiate qualitatively and quantitatively similar initial signaling

Phosphorylation of H2AX at Ser-139 to generate γ-H2AX is an early cellular response to a DSB (7). After expression of I-*Sce*I in CHO-1xS.D8, CHO-2xS.Ds8, CHO-2xS.D12, CHO-2xS.R14, and CHO-4xS.R12 cells, clearly detectable γ-H2AX foci form in cells fixed and analyzed 8, 12 and 24 h later (Figure 6A). The maximum number of γ-H2AX foci scored (after subtraction of background foci measured

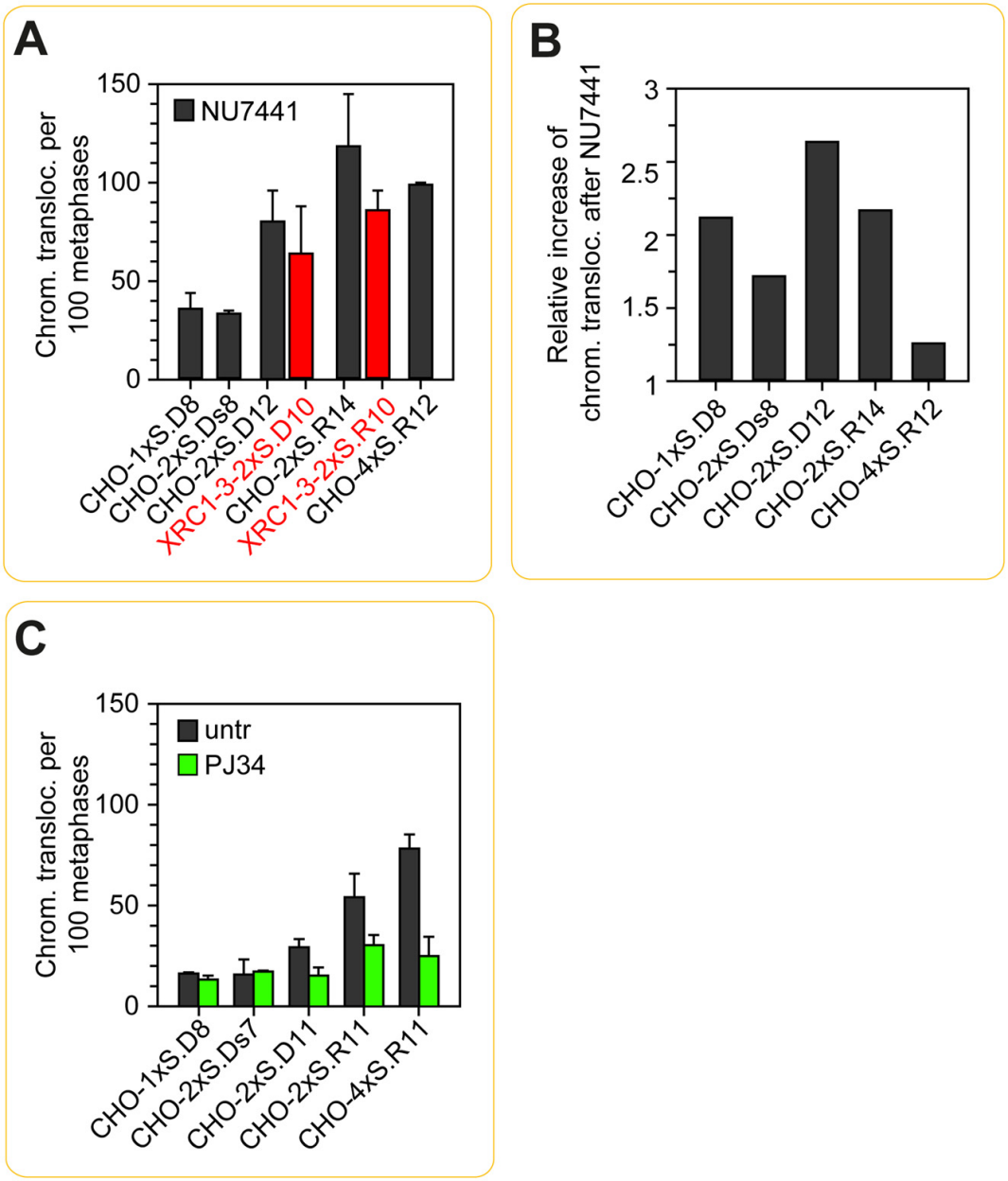

Figure 5. Chromosomal translocation formation in the indicated clones 24 h after expression of I-*Sce*I and continuous treatment with 5 μM NU7441 to compromise DNA-PKcs and thus c-NHEJ. (**A**) Chromosomal translocation formation determined in three experiments; mean ± SE are shown. Chromosomal translocations measured in mock-transfected cells have been subtracted (0–4 per 100 metaphases). (**B**) Relative increase in translocation-formation in the indicated CHO clones after treatment with NU7441. The level of chromosomal translocations in untreated cells from Figure 4C was used as basis for the normalization. (**C**) Effect of Parp1 inhibition with 10 μM PJ34 on translocation-formation in the indicated clones. Average ± SE from three experiments is shown. Translocations measured in mock-transfected cells have been subtracted.

in mock-transfected cells) is close to the number of single-DSBs or DSB-clusters present in the tested cell lines, and there is no obvious difference in foci size between single DSBs and DSB-clusters. We conclude that the majority of I-*Sce*I sites is indeed digested by the expressed restriction endonuclease, and that DSB recognition and initiation of DDR signaling, as represented here by γ-H2AX foci formation, is equally efficient on single-DSBs and DSB-clusters of different complexity. Furthermore, it is evident that each DSB-cluster forms a single γ-H2AX focus that is practically indistinguishable from the γ-H2AX focus formed by single-DSBs.

The persistence of γ-H2AX foci 24 h after transfection likely reflects repeated restriction by I-*Sce*I that prolongs the signal generated by the DSB. The reduction noted between 12 and 24 h may reflect attenuation of this digestion, repair, as well as misrepair events altering the I-*Sce*I recognition sequence and stopping further restriction. Reduction in I-*Sce*I expression is an unlikely cause, as I-*Sce*I levels re-

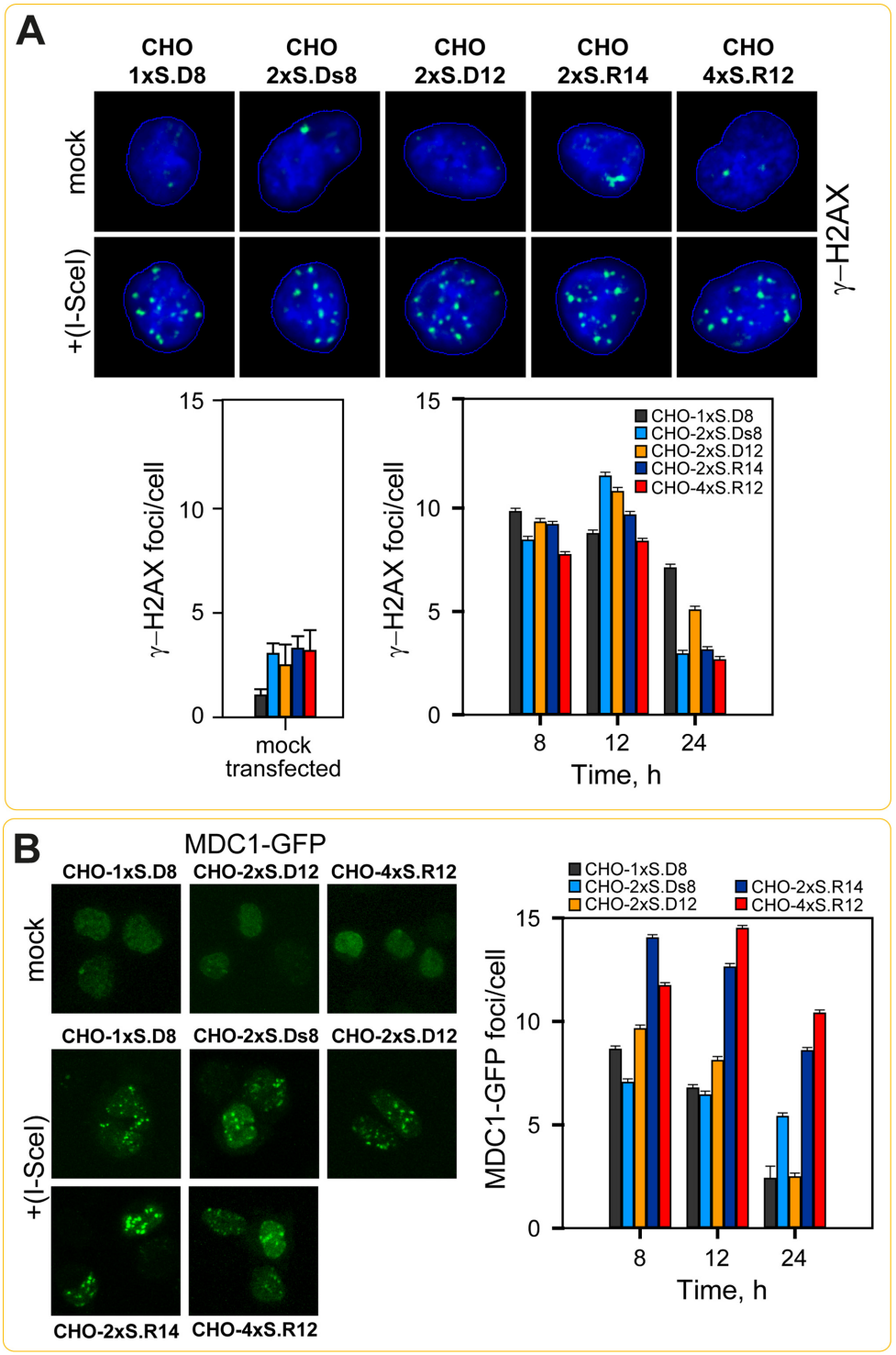

Figure 6. Activation of DDR after transient expression in the indicated CHO clones of I-*Sce*I. (**A**) Formation of γ-H2AX foci at I-*Sce*I mediated single-DSBs and DSB-clusters. Upper panel: Representative immunofluorescent images of γ-H2AX foci generated 8 h after transfection. Lower right panel: Quantitative analysis showing averages ± SE from 3 independent experiments of γ-H2AX foci formation in mock transfected and I-*Sce*I transfected cells. The number of foci scored in I-*Sce*I transfected cells is background subtracted (shown in lower left panel). (**B**) Live cell imaging experiments analyzing formation of MDC1-GFP foci after I-*Sce*I expression in the indicated CHO clones. Left panel: representative live cell images, right panel: quantitative analysis of MDC1-GFP foci. Data show the background subtracted average ± SE from three independent experiments.

main high up to 72 h after transfection (Supplementary Figure S1A).

Live-cell imaging uncovers marked differences in late DNA damage signaling between single-DSBs and DSB-clusters

Analysis of MDC1 localization at DSB sites by live-cell imaging up to 24 h after I-*Sce*I and MDC1-GFP co-expression gives foci formation results that parallel those of γ-H2AX (Figure 6B). Here again, the maximum number of MDC1 foci scored approaches the numbers of single-DSBs and DSB-clusters present in the cells. Thus, simple-DSBs and DSB-clusters provoke similar MDC1 accretion to the break sites.

Further downstream the DSB signaling cascade, the mediator protein 53BP1 is recruited to DSBs. 53BP1 accumulates over a 1 Mb region of chromatin and its recruitment requires independent inputs from a complex cascade of events that include the recruitment of upstream protein components, the modification of proteins associated with chromatin and the removal of proteins constitutively associated with undamaged chromatin (50). To analyze 53BP1 foci formation after the induction of single-DSBs and DSB-clusters, we co-expressed I-*Sce*I and GFP-53BP1 and followed cells by live-cell imaging. Supplementary Figure S3 shows that in the example of the clones CHO-1xS.D8 and CHO-2xS.R14, GFP-53BP1 protein is expressed at levels roughly twice higher than those of the endogenous 53BP1 protein, detected in mock transfected cells.

53BP1 foci scoring in clones sustaining single-DSBs or DSB-pairs with compatible apical ends generates the results summarized in Figure 7A. Notably, only relatively few 53BP1 foci (less than 50% of the expected) are detectable above background in this experimental setup at any time. On the other hand, 53BP1 foci develop at nearly 80% of the expected levels in cells harboring I-*Sce*I quadruplets and I-*Sce*I-pairs generating incompatible apical ends (Figure 7B). This gradually increasing accretion of 53BP1 to DSB-clusters *versus* single-DSBs is the first demonstration that late signaling intensity and its spreading in chromatin depend on the complexity of the underlying DSB cluster. Together with the results discussed above on translocation-formation, they suggest enhanced 53BP1 accretion when chromatin breaks evolve in ways favoring processing by alt-EJ.

If enhanced accretion of 53BP1 marks DSBs that evolve in ways favoring processing by alt-EJ, one can predict that inhibition of c-NHEJ with NU7441 will enhance 53BP1 accretion during processing of single-DSBs, or DSB pairs with compatible apical ends. To test this postulate, we treated cells immediately after transfection with 5 μM NU7441.

Notably, after treatment with NU7441, clearly more 53BP1 foci develop in cells harboring single I-*Sce*I integration sites, or I-*Sce*I pairs generating compatible apical ends (Figure 7C). In contrast, treatment with NU7441 of cells with integrations of I-*Sce*I quadruplets, or I-*Sce*I pairs generating incompatible apical ends has only a modest effect on 53BP1 foci development (Figure 7D).

The trends noted here after treatment with NU7411 are also recapitulated in XRC1-3 cells analyzed in the absence of inhibitor. Indeed XRC1-3-2xS.R10 harboring ten integrations of I-*Sce*I pairs generating incompatible apical ends develop 53BP1 foci at numbers even beyond the expected number of integrations (Figure 7E). In contrast, XRC1-3-2xS.D10 cells harboring ten integrations of I-*Sce*I pairs generating compatible ends show a significantly lower number of 53BP1 foci (Figure 7E). Collectively, these observations uncover a dependence of 53BP1 accretion on DSB clustering that parallels the observed propensity for processing by alt-EJ.

Immunofluorescence staining of 53BP1 in fixed cells and parallel comparison with γ-H2AX foci shows trends similar to those presented above. Indeed, more γ-H2AX foci form in general in our clones than 53BP1 foci, but these numbers approach each other in the case of clones harboring DSB clusters. Yet, the differences between γ-H2AX and 53BP1 foci formation are smaller here than it can be inferred from the live cell imaging experiments described above (Figure 7F). We attribute this difference to inherent characteristics to the two methodologies. Immunofluorescence staining is likely detecting 53BP1 foci with higher sensitivity, due to the lower background achieved by the extraction step included in the protocol. On the other hand, live-cell imaging clearly detects quantitative increases in 53BP1 accretion to DSB-clusters that is not directly evident by immunofluorescence—probably due to 53BP1 signal loss during the extraction step.

We conclude that DSB clusters, even when generated within a few hundred bp, cause 53BP1 accretion that is likely to extend over several million bp and being markedly more extensive than that caused by single DSBs.

DISCUSSION

The speed with which cells of higher eukaryotes process DSBs, even when these are present at levels far beyond what one would consider physiologically-relevant is astonishing, particularly when considering the severity of the DSB as a DNA lesion and the markedly slower processing speeds of other, 'simpler', DNA lesions (8). Central role in this feat takes c-NHEJ, with its high speed tuned to mainly benefit rejoining of the directly adjacent ends of a DSB; sequence at the generated junction is actually frequently sacrificed. Direct benefit for the cell with this solution is arguably the suppression of chromosomal translocations.

Translocations are generated when the ends of two or more DSBs are rejoined in ways that generate new combinations in the genome (6,8–10). They represent errors, or more likely accidents in the processing of DSBs. Since HRR is unlikely to catalyze their formation, c-NHEJ and alt-EJ become natural candidates, with alt-EJ featuring more prominently, although the actual relative contribution is debated and likely to also be cell-cycle-phase and DSB-site dependent (16,44,51).

Requirement for translocation-formation is that the ends of the participating DSBs, which for each DSB at induction are directly adjacent and therefore privileged for rejoining, drift apart and join with ends from neighboring DSBs also experiencing processing complications (39–41,52). The number of available DSBs for end exchange will also critically affect translocation-formation. Since processing by HRR or c-NHEJ will counteract DNA end-drifting, when

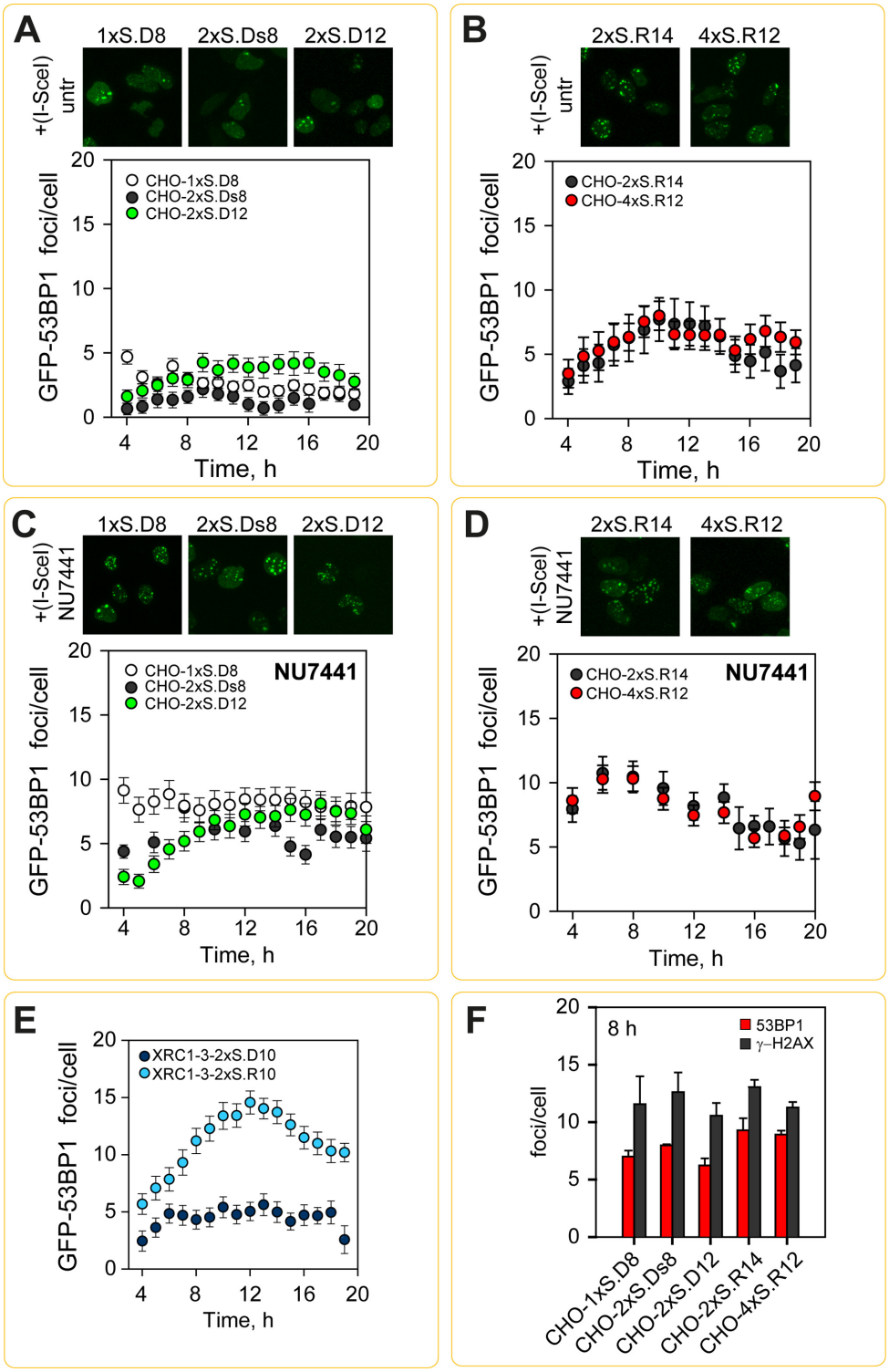

Figure 7. Differential recruitment of GFP-53BP1 protein at single-DSBs and DSB-clusters. (**A**) Live-cell imaging of GFP-53BP1 foci 4–20 h after co-transfection of the indicated cell lines with GFP-53BP1 and I-*Sce*I expressing plasmids. The pGFP-53BP1 plasmid expresses a truncated 53BP1, fused to GFP protein (see Supplementary Figure S3). Quantitative analysis compiling results from three independent experiments in the indicated CHO clones. Results shown are background subtracted and represent average ± SE from three independent experiments. (**B**) As in panel (A) for cells harboring I-*Sce*I integrations generating DSB pairs with incompatible apical DNA ends, or DSB quadruplets. (**C** and **D**) As in panels (A), (B) for cells treated with NU7441. (**E**) As A for XRC1-3-2xS.D10 and XRC1-3-2xS.R10 cells. (**F**) Indirect immunofluorescence analysis of γ-H2AX and 53BP1 foci formation in CHO clones transfected with I-*Sce*I expression plasmid. Cells were processed 8 h after transfection. The results are background subtracted and show results from 3 independent experiments as average ± SE.

it happens, drifting may be the result of an accident caused by a failure of these repair pathways to engage, or by processes unrelated to the repair event (10,52).

Several processes can cause drifting of DSB ends. First, impaired DSB processing, globally or locally, will increase the time ends remain open and thus the chance to drift apart by diffusion, or by the programmed chromatin changes described next (10,52). Second, ongoing activities on chromatin, such as transcription and replication, as well as general and local chromatin remodeling, including scheduled global condensation/decondensation (e.g. before or after mitosis), can unintentionally force end-drifting even in repair proficient cells. In addition, and relevant to the present work, drifting of DNA ends may be facilitated by chromatin destabilization generated by DSB-clusters such as those studied here.

The low induction from single-DSBs of cell killing and chromosome aberrations demonstrates that existing repair pathways are well-equipped to process this lesion, while suppressing the formation of translocations. However, incubation with a DNA-PKcs inhibitor, markedly increases translocation-formation, demonstrating the importance of speedy processing, specifically by c-NHEJ, in the suppression of translocation-formation - as also shown in a recent study (52).

Notably, the ability of DSB repair systems to suppress translocations is reduced when DSBs present in the form of clusters of two, particularly when they generate incompatible apical ends, and is practically abolished in clusters of four. Since in the latter setting c-NHEJ inhibition causes no further increase in translocations, we infer that DSB quadruplets leading to translocation-formation cannot be processed by c-NHEJ. Importantly, DSB quadruplets and doublets leading to translocations frequently utilize alt-EJ, as alt-EJ inhibition using a Parp1 inhibitor markedly reduces their formation. We conclude that DSB-pairs, but particularly DSB-quadruplets destabilize chromatin and facilitate drifting of DNA ends that feeds translocation-formation. Further, we conclude that alt-EJ operates on destabilized chromatin more efficiently than c-NHEJ and is predominantly responsible for translocation-formation in our experimental system.

The marked differences in processing and translocation-formation observed between single-DSBs and DSB-doublets suggests that I-*Sce*I-based model systems featuring single and double I-*Sce*I sites will not generate equivalent data regarding pathway utilization or propensity for error-prone processing. Presently, this parameter is not considered in the interpretation of results generated using such systems, and constructs with single or pairs of I-*Sce*I sites are considered equivalent in terms of processing possibilities and outcomes.

Our observations offer important insights explaining the increased efficacy of forms of radiation imparting energy with ionization density (LET) higher than X-rays or gamma rays. It has been known for some time that while wild-type cells are killed by high LET radiation markedly more efficiently than by low LET radiation, c-NHEJ deficient cells are killed by high and low LET radiation with the same efficiency. A mechanistic explanation for this response is presently lacking. One model postulates that this is due to the generation of small (∼40 bp) DNA fragments that inhibit c-NHEJ by preventing the normal function of Ku (53). We propose that the effect actually derives from the generation by high LET radiation of DSB-clusters that compromise c-NHEJ as demonstrated here, independently of whether Ku can bind to the generated fragments or not.

It is notable that as DNA-PKcs inhibition brings the translocation yields of single-DSBs to the level constitutively seen by DSB-quadruplets, with or without inhibitors, DNA-PKcs inhibition brings cell killing of low LET radiation to levels observed after exposure to high LET radiation, irrespectively of inhibitor treatment. It should be noted however, that while IR-induced DSBs are generated only once in the cell, within a rather short period of time and are typically not directly ligatable, I-*Sce*I-mediated induction of DSBs is a prolonged, indefinitely repeatable process with direct ligation sufficient for repair.

A striking observation is that the level of 53BP1 accretion, and thus possibly also its function and extent in chromatin, depends on the complexity of the underlying DSB cluster. 53BP1-foci formation is γ-H2AX and H4K20 dimethylation dependent and spans large chromatin regions in the vicinity of the break. Notably, 53BP1 is involved in long range intrachromosomal V(D)J recombination and CSR (54), as well as in the fusion between dysfunctional telomeres (55). Therefore it is thought that 53BP1 serves as a synapsis factor to mediate long range joining of distant DNA breaks. Our results suggest that 53BP1 is also recruited to facilitate processing of DSB-clusters with rather proximate DSBs (∼500 bp apart). We propose that in this setting 53BP1 recognizes destabilized regions of chromatin and supports their stabilization. However, this stabilization appears to benefit alt-EJ more directly than c-NHEJ.

It has been proposed that 53BP1 protects DNA ends from end resection favoring thus c-NHEJ while preventing alt-EJ and HRR (56). Our results suggest that recruitment of 53BP1 is compatible with alt-EJ in DSB-clusters. Moreover, recent work suggests that 53BP1 plays a role in DSB pathway selection by blocking 5′ end resection with the help of Rif1 (56–59). Indeed, 53BP1 may suppress HRR to reduce processing that requires precision and complex DNA–protein interactions in destabilized chromatin regions in order to protect genomic integrity even in the presence of DSB-clusters.

In aggregate, we provide strong direct evidence that DSB clustering and thus chromothripsis is a relevant parameter of DSB complexity. We show a suppression by DSB-clustering of c-NHEJ accompanied by increased 53BP1-accretion, alt-EJ-utilization and translocation-formation. DSB clusters generated at distances of about 200 bp appear more effective than those generated at shorter distances. Our observations explain the enhanced adverse effects of forms of radiation such as radon and space radiation, and define DSB-clustering as a determinant of radiation-induced cell killing and possibly also carcinogenesis.

SUPPLEMENTARY DATA

Supplementary Data are available at NAR Online.

ACKNOWLEDGEMENTS

Special thanks go to Dr. Zoltan Ivics for providing the Sleeping Beauty Reagents and for advice in their use. We also thanks Drs. T. Halazonetis and J. Bartek for constructs.

FUNDING

BMBF [02NUK043B-COLLAR]; DFG [GRK1739]. Funding for open access charge: Institutional Funds.
Conflict of interest statement. None declared.

REFERENCES

1. Zhou,B.B. and Elledge,S.J. (2000) The DNA damage response: putting checkpoints in perspective. *Nature*, **408**, 433–439.
2. Jackson,S.P. and Bartek,J. (2009) The DNA-damage response in human biology and disease. *Nature*, **461**, 1071–1078.
3. Berens,T.J. and Toczyski,D.P. (2012) Keeping It Together in Times of Stress: Checkpoint Function at Stalled Replication Forks. *Mol. Cell*, **45**, 585–586.
4. Burrell,R.A., McClelland,S.E., Endesfelder,D., Groth,P., Weller,M.-C., Shaikh,N., Domingo,E., Kanu,N., Dewhurst,S.M., Gronroos,E. *et al.* (2013) Replication stress links structural and numerical cancer chromosomal instability. *Nature*, **494**, 492–496.
5. Mortusewicz,O., Herr,P. and Helleday,T. (2013) Early replication fragile sites: where replication-transcription collisions cause genetic instability. *EMBO J.*, **32**, 493–495.
6. Alt,F.W., Zhang,Y., Meng,F.-L., Guo,C. and Schwer,B. (2013) Mechanisms of Programmed DNA Lesions and Genomic Instability in the Immune System. *Cell*, **152**, 417–429.
7. Kinner,A., Wu,W., Staudt,C. and Iliakis,G. (2008) γ-H2AX in recognition and signaling of DNA double-strand breaks in the context of chromatin. *Nucleic Acids Res.*, **36**, 5678–5694.
8. Schipler,A. and Iliakis,G. (2013) DNA double-strand-break complexity levels and their possible contributions to the probability for error-prone processing and repair pathway choice. *Nucleic Acids Res.*, **41**, 7589–7605.
9. Bunting,S.F. and Nussenzweig,A. (2013) End-joining, translocations and cancer. *Nat. Rev. Cancer*, **13**, 443–454.
10. Roukos,V. and Misteli,T. (2014) The biogenesis of chromosome translocations. *Nat. Cell Biol.*, **16**, 293–300.
11. Mladenov,E. and Iliakis,G. (2011) Induction and repair of DNA double strand breaks: the increasing spectrum of non-homologous end joining pathways. *Mutat. Res.*, **711**, 61–72.
12. Heyer,W.-D., Ehmsen,K.T. and Liu,J. (2010) Regulation of homologous recombination in eukaryotes. *Annu. Rev. Genet.*, **44**, 113–139.
13. Mladenov,E., Magin,S., Soni,A. and Iliakis,G. (2013) DNA double-strand break repair as determinant of cellular radiosensitivity to killing and target in radiation therapy. *Front. Oncol.*, **3**, 113.
14. Iliakis,G., Wang,H., Perrault,A.R., Boecker,W., Rosidi,B., Windhofer,F., Wu,W., Guan,J., Terzoudi,G. and Pantelias,G. (2004) Mechanisms of DNA double strand break repair and chromosome aberration formation. *Cytogenet. Genome Res.*, **104**, 14–20.
15. Lieber,M.R. (2010) The mechanism of double-strand DNA break repair by the nonhomologous DNA end-joining pathway. *Annu. Rev. Biochem.*, **79**, 1.1–1.31.
16. Soni,A., Siemann,M., Pantelias,G.E. and Iliakis,G. (2015) Marked cell cycle-dependent contribution of alternative end joining to formation of chromosome translocations by stochastically induced DNA double strand breaks in human cells. *Mutat. Res.*, **793**, 2–8.
17. Aziz,K., Nowsheen,S., Pantelias,G., Iliakis,G., Gorgoulis,V.G. and Georgakilas,A.G. (2012) Targeting DNA damage and repair: embracing the pharmacological era for successful cancer therapy. *Pharmacol. Ther.*, **133**, 334–350.
18. Stephens,P.J., Greenman,C.D., Fu,B., Yang,F., Rignell,G.R., Mudie,L.J., Pleasance,E.D., Lau,K.W., Beare,D., Stebbings,L.A. *et al.* (2011) Massive genomic rearrangement acquired in a single catastrophic event during cancer development. *Cell*, **144**, 27–40.
19. Forment,J.V., Kaidi,A. and Jackson,S.P. (2012) Chromothripsis and cancer: causes and consequences of chromosome shattering. *Nat. Rev. Cancer*, **12**, 663–670.
20. Kloosterman,W.P., Tavakoli-Yaraki,M., van Roosmalen,M.J., van Binsbergen,E., Renkens,I., Duran,K., Ballarati,L., Vergult,S., Giardino,D., Hansson,K. *et al.* (2012) Constitutional chromothripsis rearrangements involve clustered double-stranded DNA breaks and nonhomologous repair mechanisms. *Cell Rep.*, **1**, 648–655.
21. Molenaar,J.J., Koster,J., Zwijnenburg,D.A., van Sluis,P., Valentijn,L.J., van der Ploeg,I., Hamdi,M., van Nes,J., Westerman,B.A., van Arkel,J. *et al.* (2012) Sequencing of neuroblastoma identifies chromothripsis and defects in neuritogenesis genes. *Nature*, **483**, 589–593.
22. Pang,D., Winters,T.A., Jung,M., Purkayastha,S., Cavalli,L.R., Chasovkikh,S., Haddad,B.R. and Dritschilo,A. (2011) Radiation-generated Short DNA fragments may perturb non-homologous end-joining and induce genomic instability. *J. Radiat. Res.*, **52**, 309–319.
23. Johnston,P.J., Olive,P.L. and Bryant,P.E. (1997) Higher-order chromatin structure-dependent repair of DNA double-strand breaks: modeling the elution of DNA from nucleoids. *Radiat. Res.*, **148**, 561–567.
24. Wang,H., Zhang,X., Wang,P., Yu,X., Essers,J., Chen,D., Kanaar,R., Takeda,S. and Wang,Y. (2010) Characteristics of DNA-binding proteins determine the biological sensitivity to high-linear energy transfer radiation. *Nucleic Acids Res.*, **38**, 3245–3251.
25. Friedland,W., Dingfelder,M., Kundrát,P. and Jacob,P. (2011) Track structures, DNA targets and radiation effects in the biophysical Monte Carlo simulation code PARTRAC. *Mutat. Res./Fundam. Mol. Mech. Mutagen.*, **711**, 28–40.
26. Holley,W.R. and Chatterjee,A. (1996) Clusters of DNA damage induced by ionizing radiation: Formation of short DNA fragments. 1. Theoretical modeling. *Radiat. Res.*, **145**, 188–199.
27. Höglund,E. and Stenerlöw,B. (2001) Induction and rejoining of DNA double-strand breaks in normal human skin fibroblasts after exposure to radiation of different linear energy transfer: possible roles of track structure and chromatin organization. *Radiat. Res.*, **155**, 818–825.
28. Rydberg,B. (1996) Clusters of DNA damage induced by ionizing radiation: formation of short DNA fragments. 11. Experimental detection. *Radiat. Res.*, **145**, 200–209.
29. Durante,M. and Loeffler,J.S. (2010) Charged particles in radiation oncology. *Nat. Rev. Clin. Oncol.*, **7**, 37–43.
30. Durante,M. and Cucinotta,F.A. (2008) Heavy ion carcinogenesis and human space exploration. *Nat. Rev. Cancer*, **8**, 465–472.
31. Ostashevsky,J.Y. (1989) A model relating cell survival to DNA fragment loss and unrepaired double-strand breaks. *Radiat. Res.*, **118**, 437–466.
32. Ostashevsky,J.Y. (2000) Higher-order structure of interphase chromosomes and radiation-induced chromosomal exchange aberrations. *Int. J. Radiat. Biol.*, **76**, 1179–1187.
33. Fakir,H., Sachs,R.K., Stenerlöw,B. and Hofmann,W. (2006) Clusters of DNA double-strand breaks induced by different doses of nitrogen ions for various LETs: experimental measurements and theoretical analyses. *Radiat. Res.*, **166**, 917–927.
34. Ponomarev,A.L. and Cucinotta,F.A. (2006) Chromatin loops are responsible for higher counts of small DNA fragments induced by high-LET radiation, while chromosomal domains do not affect the fragment sizes. *Int. J. Radiat. Biol.*, **82**, 293–305.
35. Friedrich,T., Durante,M. and Scholz,M. (2012) Modeling cell survival after photon irradiation based on double-strand break clustering in megabase pair chromatin loops. *Radiat. Res.*, **178**, 385–394.
36. Dudley,D.D., Chaudhuri,J., Bassing,C.H. and Alt,F.W. (2005) Mechanism and Control of V(D)J Recombination versus Class Switch Recombination: Similarities and Differences. *Adv. Immunol.*, **86**, 43–112.
37. Boboila,C., Alt,F.W. and Schwer,B. (2012) Classical and Alternative End-Joining Pathways for Repair of Lymphocyte-Specific and General DNA Double-Strand Breaks. *Adv. Immunol.* ,**116**, 1–49.
38. Zhang,Y., McCord,R.P., Ho,Y.-J., Lajoie,B.R., Hildebrand,D.G., Simon,A.C., Becker,M.S., Alt,F.W. and Dekker,J. (2012) Spatial organization of the mouse genome and its role in recurrent chromosomal translocations. *Cell*, **148**, 908–921.
39. Chiarle,R., Zhang,Y., Frock,R.L., Lewis,S.M., Molinie,B., Ho,Y.-J., Myers,D.R., Choi,V.W., Compagno,M., Malkin,D.J. *et al.* (2011) Genome-wide translocation sequencing reveals mechanisms of

chromosome breaks and rearrangements in B cells. *Cell*, **147**, 107–119.
40. Hakim,O., Resch,W., Yamane,A., Klein,I., Kieffer-Kwon,K.-R., Jankovic,M., Oliveira,T., Bothmer,A., Voss,T.C., Ansarah-Sobrinho,C. *et al.* (2012) DNA damage defines sites of recurrent chromosomal translocations in B lymphocytes. *Nature*, **484**, 69–74.
41. Klein,I.A., Resch,W., Jankovic,M., Oliveira,T., Yamane,A., Nakahashi,H., Di Virgilio,M., Bothmer,A., Nussenzweig,A., Robbiani,D.F. *et al.* (2011) Translocation-capture sequencing reveals the extent and nature of chromosomal rearrangements in B lymphocytes. *Cell*, **147**, 95–106.
42. Besaratinia,A. and Pfeifer,G.P. (2009) DNA-lesion mapping in mammalian cells. *Methods*, **48**, 35–39.
43. Weinstock,D.M., Nakanishi,K., Helgadottir,H.R. and Jasin,M. (2006) Assaying double-strand break repair pathway choice in mammalian cells using a targeted endonuclease or the RAG recombinase. *Methods Enzymol.*, **409**, 524–540.
44. Iliakis,G., Murmann,T. and Soni,A. (2015) Alternative end-joining repair pathways are the ultimate backup for abrogated classical non-homologous end-joining and homologous recombination repair: Implications for the formation of chromosome translocations. *Mutat. Res./Genet. Toxicol. Environ. Mutagen.*, **793**, 166–175.
45. Izsvak,Z. and Ivics,Z. (2004) Sleeping beauty transposition: biology and applications for molecular therapy. *Mol. Ther.*, **9**, 147–156.
46. Ivics,Z., Hackett,P.B., Plasterk,R.H. and Izsvak,Z. (1997) Molecular recontruction of sleeping beauty, a Tc1-like transposon from fish, and its transposition in human cells. *Cell*, **91**, 501–510.
47. Hlatky,L., Sachs,R.K., Vazquez,M. and Cornforth,M.N. (2002) Radiation-induced chromosome aberrations: insights gained from biophysical modeling. *Bioessays*, **24**, 714–723.
48. Soni,A., Siemann,M., Grabos,M., Murmann,T., Pantelias,G.E. and Iliakis,G. (2014) Requirement for Parp-1 and DNA ligases 1 or 3 but not of Xrcc1 in chromosomal translocation formation by backup end joining. *Nucleic Acids Res.*, **42**, 6380–6392.
49. Wang,M., Wu,W., Wu,W., Rosidi,B., Zhang,L., Wang,H. and Iliakis,G. (2006) PARP-1 and Ku compete for repair of DNA double strand breaks by distinct NHEJ pathways. *Nucleic Acids Res.*, **34**, 6170–6182.
50. Panier,S. and Boulton,S.J. (2014) Double-strand break repair: 53BP1 comes into focus. *Nat. Rev. Mol. Cell Biol.*, **15**, 7–18.
51. Ghezraoui,H., Piganeau,M., Renouf,B., Renaud,J.-B., Sallmyr,A., Ruis,B., Oh,S., Tomkinson,A.E., Hendrickson,Eric A., Giovannangeli,C. *et al.* (2014) Chromosomal translocations in human cells are generated by canonical nonhomologous end-joining. *Mol. Cell*, **55**, 829–842.
52. Roukos,V., Voss,T.C., Schmidt,C.K., Lee,S., Wangsa,D. and Misteli,T. (2013) Spatial dynamics of chromosome translocations in living cells. *Science*, **341**, 660–664.
53. Wang,H., Wang,X., Zhang,P. and Wang,Y. (2008) The Ku-dependent non-homologous end-joining but not other repair pathway is inhibited by high linear energy transfer ionizing radiation. *DNA Repair*, **7**, 725–733.
54. Difilippantonio,S., Gapud,E., Wong,N., Huang,C.-Y., Mahowald,G., Chen,H.T., Kruhlak,M.J., Callen,E., Livak,F., Nussenzweig,M.C. *et al.* (2008) 53BP1 facilitates long-range DNA end-joining during V(D)J recombination. *Nature*, **456**, 529–533.
55. Dimitrova,N., Chen,Y.-C.M., Spector,D.L. and de Lange,T. (2008) 53BP1 promotes non-homologous end joining of telomeres by increasing chromatin mobility. *Nature*, **456**, 524–528.
56. Bothmer,A., Robbiani,D.F., Feldhahn,N., Gazumyan,A., Nussenzweig,A. and Nussenzweig,M.C. (2010) 53BP1 regulates DNA resection and the choice between classical and alternative end joining during class switch recombination. *J Exp Med*, **207**, 855–865.
57. Bunting,S.F., Callén,E., Wong,N., Chen,H.-T., Polato,F., Gunn,A., Bothmer,A., Feldhahn,N., Fernandez-Capetillo,O., Cao,L. *et al.* (2010) 53BP1 inhibits homologous recombination in Brca1-deficient cells by blocking resection of DNA breaks. *Cell*, **141**, 243–254.
58. Zimmermann,M., Lottersberger,F., Buonomo,S.B., Sfeir,A. and de Lange,T. (2013) 53BP1 regulates DSB repair using Rif1 to control 5′ end resection. *Science*, **339**, 700–704.
59. Gupta,A., Hunt,C.R., Hegde,M.L., Chakraborty,S., Udayakumar,D., Horikoshi,N., Singh,M., Ramnarain,D.B., Hittelman,W.N., Namjoshi,S. *et al.* (2014) MOF phosphorylation by ATM regulates 53BP1-mediated double-strand break repair pathway choice. *Cell Rep.*, **8**, 177–189.